

Publications

4-22-2019

Gravity Wave Ducting Observed in the Mesosphere Over Jicamarca, Peru

Gerald A. Lehmacher
Clemson University, glehmac@clemson.edu

Christopher J. Heale
Embry-Riddle Aeronautical University, HEALEC@erau.edu

Jonathan B. Snively
Embry-Riddle Aeronautical University, snivelyj@erau.edu

Erhan Kudeki
University of Illinois at Urbana-Champaign

Pablo M. Reyes
University of Illinois at Urbana-Champaign

See next page for additional authors

Follow this and additional works at: <https://commons.erau.edu/publication>



Part of the [Atmospheric Sciences Commons](#)

Scholarly Commons Citation

Lehmacher, G. A., Kudeki, E., Reyes, P. M., Lee, K., Heale, C. J., & Snively, J. B. (2019). Gravity wave ducting observed in the mesosphere over Jicamarca, Peru. *Journal of Geophysical Research: Atmospheres*, 124, 5166–5177. <https://doi.org/10.1029/2019JD030264>

This Article is brought to you for free and open access by Scholarly Commons. It has been accepted for inclusion in Publications by an authorized administrator of Scholarly Commons. For more information, please contact commons@erau.edu.

Authors

Gerald A. Lehmacher, Christopher J. Heale, Jonathan B. Snively, Erhan Kudeki, Pablo M. Reyes, and Kiwook Lee

JGR Atmospheres

RESEARCH ARTICLE

10.1029/2019JD030264

Key Points:

- Quasi-monochromatic gravity waves are observed propagating in the equatorial middle mesosphere, likely in a Doppler duct
- The waves extend through an upper evanescent layer, propagating in a second stable layer above the duct
- Displacement of radar scattering layer and measured vertical velocity match the oscillatory motion of a wave near reflection

Correspondence to:

G. A. Lehmacher,
glehmac@clermson.edu

Citation:

Lehmacher, G. A., Kudeki, E., Reyes, P. M., Lee, K., Heale, C. J., & Snively, J. B. (2019). Gravity wave ducting observed in the mesosphere over Jicamarca, Peru. *Journal of Geophysical Research: Atmospheres*, 124, 5166–5177. <https://doi.org/10.1029/2019JD030264>

Received 20 JAN 2019

Accepted 15 APR 2019

Accepted article online 22 APR 2019

Published online 21 MAY 2019

Author Contributions

Data curation: Pablo M. Reyes

Funding Acquisition: Gerald A. Lehmacher, Erhan Kudeki

Methodology: Gerald A. Lehmacher

Software: Gerald A. Lehmacher, Erhan Kudeki, Pablo M. Reyes, Kiwook Lee,





Christopher J. Heale

Writing - Original Draft: Gerald A. Lehmacher

Investigation: Gerald A. Lehmacher

Writing - review & editing: Gerald A. Lehmacher, Erhan Kudeki, Jonathan B. Snively

Gravity Wave Ducting Observed in the Mesosphere Over Jicamarca, Peru

Gerald A. Lehmacher¹ , Erhan Kudeki² , Pablo M. Reyes^{2,3} , Kiwook Lee², Christopher J. Heale⁴ , and Jonathan B. Snively⁴ 

¹Department of Physics and Astronomy, Clemson University, Clemson, SC, USA, ²Department of Electrical and Computer Engineering, University of Illinois at Urbana-Champaign, Urbana, IL, USA, ³SRI International, Menlo Park, CA, USA, ⁴Department of Physical Sciences, Embry-Riddle Aeronautical University, Daytona Beach, FL, USA

Abstract Short-period gravity waves are ubiquitous in the mesosphere, but the vertical structures of their perturbations are difficult to observe. The Jicamarca 50-MHz very high frequency radar allows observations of winds and turbulent scatter with high temporal and vertical resolution. We present a case of a quasi-monochromatic gravity wave with period 520 (± 40) s that is likely ducted below a southward wind jet between 68 and 74 km. Above this layer of evanescence, a northward wind enables it to emerge into a more stable layer, where it is refracted to a short vertical wavelength of 2.2 (± 0.2) km; data show evidence of weak nonlinearity, and possible overturning or partial reflection from higher altitudes, above the observable region, in the form of a standing wave structure in vertical velocity at approximately 75 km. Based on the dispersion relation, and with help of a two-dimensional model, we determine that most likely the wave is propagating northward and is being ducted below and tunneling through the regions of evanescence created by the wind flow and typical mesospheric thermal structure. This is the first time that such an event has been identified in the Jicamarca mesospheric echoes, and it is distinct from Kelvin-Helmholtz billows also commonly seen with this sensitive radar—instead apparently revealing tunneling of the gravity wave through ambient winds.

1. Introduction

Atmospheric gravity waves (GWs), also known as buoyancy waves, provide an important mechanism to carry fluxes of energy and momentum from the lower atmosphere into the middle and upper atmosphere and, specifically, the mesosphere and lower thermosphere. A growing number of observations, mostly from airglow imagers, find evidence that mesospheric GWs frequently travel in (and out of) ducts formed by the background temperature or wind structure. These ducted waves may appear thousands of kilometers horizontally removed from their sources in the lower atmosphere (Hickey, 2001; Pautet et al., 2005; Snively & Pasko, 2003; Taylor et al., 1997; Walterscheid et al., 1999). A study by Isler et al. (1997) suggests that at midlatitudes 75% of the observed waves may be ducted, while observations at a southern high-latitude site found only 5% of ducted waves (Nielsen et al., 2012); however, Snively et al. (2013) found that many more of those waves are likely ducted albeit with boundaries outside of the observable layer. An abundance of mesospheric bores have also been reported at high latitudes (Pautet et al., 2018). The equatorial and low-latitude mesosphere is characterized by long-period inertia-gravity waves and tidal motions with large amplitudes providing conditions for wave ducting in narrow vertical regions. Measured short-period oscillations of the vertical wind at low latitudes have been associated with ducted waves directly (Fritts et al., 1992; Fritts & Janches, 2008).

GWs may encounter thermal ducts (regions typically within a local maximum in the buoyancy frequency), Doppler ducts (regions with boundaries created by Doppler shift), or a combination of such conditions (Chimonas & Hines, 1986; Eckart, 1961; Fritts & Yuan, 1989). Waves are also subject to leakage, reflection, and refraction at the boundaries (Hickey, 2001; Nappo, 2012) and may tunnel through the evanescent layers surrounding the duct (Simkhada et al., 2009; Sutherland & Yewchuk, 2004). Modeling suggests that wave energy is more effectively transmitted over large horizontal distances in the stratosphere by ducting (Heale et al., 2014). Fritts and Yuan (1989) suggested that multiple and variable ducting conditions may enable a “quasi-random vertical transfer of wave energy at high intrinsic frequencies” from the lower to the upper atmosphere. Many observations of GW ducting in the mesosphere are based on imaging of one or two

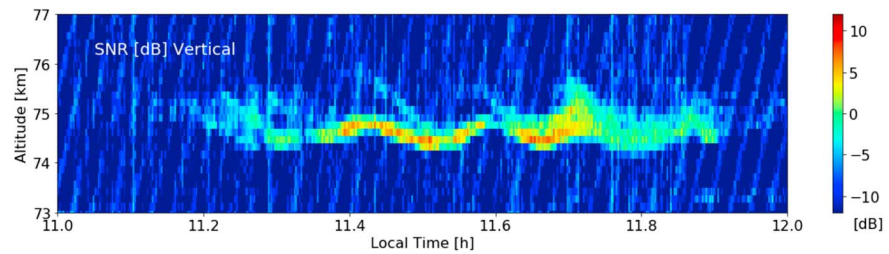


Figure 1. Signal-to-noise ratio (SNR) observed in vertical beam on 30 September 2015 between 11 and 12 LT. The vertical and temporal resolution are 150 m and 8.64 s, respectively. The faint stripes in the background are likely due to a time-varying interference signal from a very high frequency radio station, which still remained after signal decoding and processing.

airglow emission layers, especially the hydroxyl (OH) layer around 87 km and the oxygen (OI) layer around 96 km. Analysis of consecutive 2-D images yields horizontal wavelength, propagation direction, apparent frequency, and wave speed. The conditions for vertical wave propagation, namely, the vertical wavenumber m based on linear GW theory, can be calculated if wind and temperature profiles are known. Simkhada et al. (2009) presented an observational and modeling study of ducted waves over Hawaii based on airglow intensity maps and combined them with meteor radar horizontal wind profiles. Bossert et al. (2014) combined OH airglow temperature maps with winds, temperatures, and density perturbations from sodium lidar to study a GW ducting event at high latitudes. Cao et al. (2016) analyzed airglow intensity combined with temperature and vertical wind structures from sodium lidar at midlatitudes and compared them with a model simulation of a GW packet propagating through multiple ducts. Noctilucent or polar mesospheric clouds are also a well-known tracer for GW activity. A study of images obtained with the CIPS instrument on the AIM satellite revealed many waves primarily with horizontal wavelengths of less than 100 km, some of which may have been ducted (Chandran et al., 2009).

Vertical wind measurements with ultrahigh frequency or very high frequency (VHF) Doppler radars are another important method to study GW motions in the mesosphere. Coherent short-period oscillations with frequencies, $\omega \sim N$, have been reported since early measurements (Miller et al., 1978; Woodman & Guillen, 1974) and have been associated with ducted wave motions (Fritts et al., 1992). Hoppe and Fritts (1995) analyzed vertical motions in polar mesospheric summer echoes obtained with the 224-MHz European Incoherent Scatter radar at 0.2-s resolution and found periods with prominent ducted wave activity. A study by Fritts and Janches (2008) using D region incoherent scatter (ISR) spectra and radial velocities from a dual-beam experiment with the Arecibo ultrahigh frequency radar suggested several regions of wave ducting in the middle mesosphere.

Here we present new high-resolution observations from the Jicamarca VHF radar in Peru. A short-period, quasi-monochromatic wave event in the middle mesosphere lasting about 1 hr was observed in the backscatter signal and wind components. The aim of this paper is a detailed analysis of the wave propagation in relationship to the background wind profile that is measured at the same time by the same instrument. Our data suggest that the wave is likely trapped in a deep layer, bounded by a region of evanescence, the depth of which is fully measured, while also leaking out at the top of the layer giving rise to a wave that is phase shifted and propagating upward (and possibly ducted as well, depending on the state of the mesopause above). This is the first time that such an event has been identified in such detail in the low-latitude daytime mesosphere with the Jicamarca radar.

The paper is organized as follows: Section 2 describes the experimental setup and radar data processing, followed by the observations of backscatter signal and vertical and horizontal wind profiles in section 3. Section 4 discusses the propagation conditions and presents modeling results that best match the observations. Section 5 contains the summary and conclusions.

2. Experiment

The 50-MHz radar at the Jicamarca Radio Observatory in Peru (12°S, 75°W) was operated in the mesosphere-stratosphere-troposphere-incoherent-scatter-radar-equatorial-electrojet (MST-ISR-EEJ) mode, which alternates between three sets of pulses; (1) 64-baud ($64 \times 1 \mu\text{s}$) complementary-coded pulses for weak, coherent echoes from the mesosphere, stratosphere, troposphere and the 150-km region (MST); (2) 3-baud

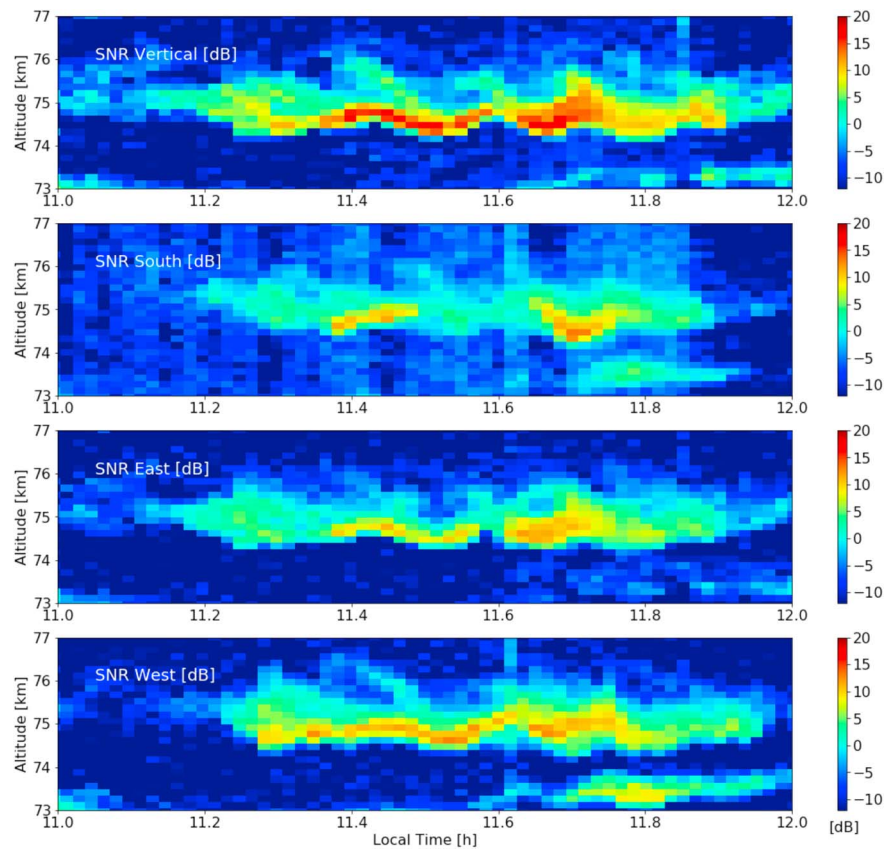


Figure 2. Signal-to-noise ratio (SNR) observed with all four beams. Same time interval as in previous figure, but time resolution is 60 s.

($3 \times 100 \mu\text{s}$) Barker-coded pulses for F ISR; and (3) $1\text{-}\mu\text{s}$ uncoded pulses for strong EEJ echoes. It is an extension of the previous MST-ISR mode (Guo et al., 2007; Lehmacher et al., 2009). Here we use only data from mesospheric altitudes sampled in the MST mode.

The antenna was configured with four beams pointing (1) vertically, (2) about 2.5° eastward and (3) westward (both perpendicular to the magnetic field) and (4) about 3.4° southward. An antenna diagram is shown in K. Lee et al. (personal communication, 2018). Complex voltages were sampled at $1 \mu\text{s}$ corresponding to a nominal range resolution of 150 m. Doppler spectra were formed with different integration times; here we use 8.64 s for signal-to-noise ratios (SNRs) and 60 s for spectral fitting with generalized Gaussian functions to determine line-of-sight (LOS) Doppler velocities and spectral widths (Sheth et al., 2006). New algorithms for more robust identification of the correct Doppler peak and the linear combination of the four LOS velocities to determine zonal, meridional, and vertical wind components are described by K. Lee et al. (personal communication, 2018).

Operation with peak pulse power of up to 2 MW at a duty cycle of 5% permits the detection of very weak mesospheric echoes caused by refractive index fluctuations at the 3-m Bragg scale. Radar cross sections (or volume reflectivities) of $< 10^{-18} \text{ m}^{-3}$ can be observed, which is still ~ 100 times larger than the incoherent scatter based on typical D region electron densities (Lehmacher et al., 2009; Woodman & Guillen, 1974). The reflectivities are generally consistent with neutral turbulent fluctuations across electron density gradients and stable temperature gradients (Lehmacher et al., 2009).

Data were collected in the MST-ISR-EEJ mode during several continuous 4-day periods since 2014. Here we present a GW event observed on 30 September 2015 between 11 and 12 hr local time (LT).

3. Observations

Figure 1 shows the SNR for the vertical beam between 11 and 12 hr LT at 8.64-s resolution. Please note that the time axis and times throughout this paper are specified in decimal fractions of hours. A narrow scattering

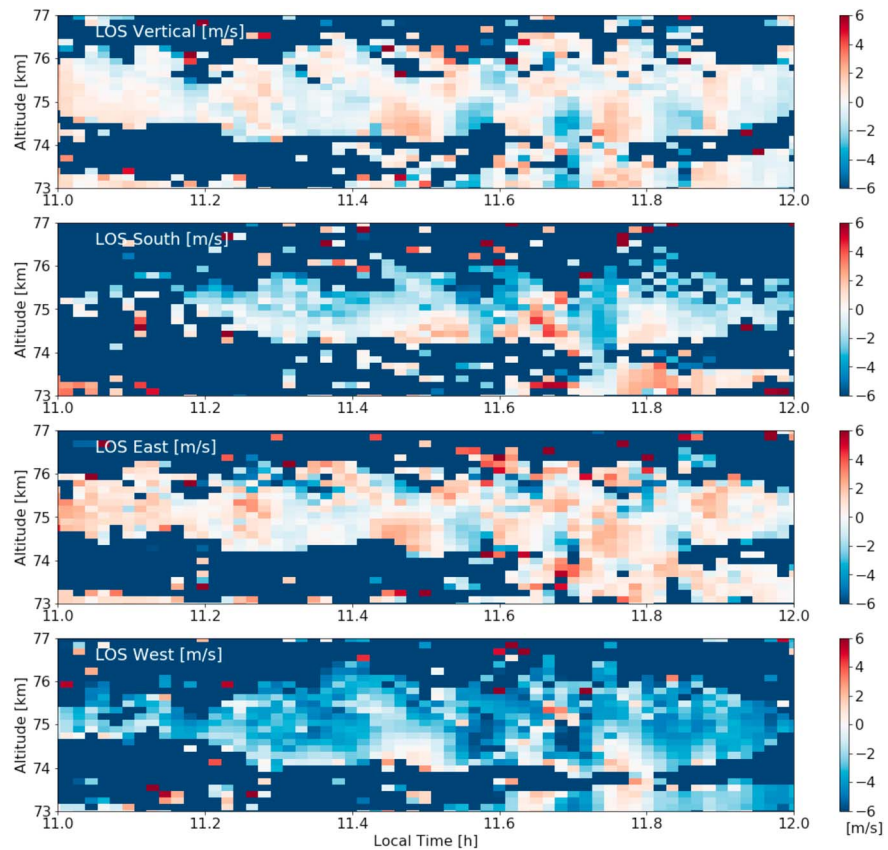


Figure 3. Line-of-sight (LOS) velocities derived from spectral fitting for all four beams. Velocities range from -6 to $+6$ m/s.

layer is detected between 74 and 75 km. It is undulated with an apparent period of $T = 520 (\pm 40)$ s and a peak-to-peak amplitude of about 450 m (about three samples at 150-m resolution). Additionally, there are downward sloping lines above the layer spaced at a similar period. At 11.5 LT, the downward sloping line seems to emerge near a layer valley. The period was estimated from 10 observations of features such as consecutive crests and valleys. The downward sloping line could indicate positions with constant phase caused by an upward propagating GW, although the perturbation does exhibit some nonlinearity, due to finite amplitude, that can also suggest tendency toward instability and wave overturning. Under the assumption that the features above the layer remain stable and are not associated with instability, the phase descends at 4.2 m/s, suggesting an upward propagating wave with vertical wavelength $\lambda_z = 2.2 (\pm 0.2)$ km above the sinusoidal layer.

The same event can be observed in all four beams in similar form as shown in Figure 2. These data were integrated over 60 s, which increases the SNR. The backscatter signal is strongest in the vertical beam and smaller in the off-vertical beams likely due to aspect sensitivity of the scattering process (Fukao, 1980; Sheth et al., 2007). The beams (beamwidth is 1°) illuminate at 75 km an area with about 1.3-km diameter. The east and west beams are about 3.2 km separated from the vertical beam and the south beam about 4.5 km. Note that the wavelike modulation of the strong scattering layer is largely in phase over these small beam separations. Larger differences are most notable in the south beam around 11.7 LT.

The LOS velocities for the three oblique beams (east, west, and south) are dominated by the vertical wind component due to their small off-zenith angles (Lee et al., 2019). This is even more so than for the dual-beam Arecibo data discussed by Fritts and Janches (2008). Figure 3 shows all four LOS velocities for the same time and range interval as in Figure 2. Despite some noise in the data, the phase coherence with the LOS velocities from the vertical beam can be observed between 11.4 and 11.6 LT where vertical winds are strongest. This is the same interval where the sinusoidal modulation of the scattering layer is most clearly visible. Again, we note deviations or a phase shift in the south beam LOS velocities around 11.7 LT. For our analysis of

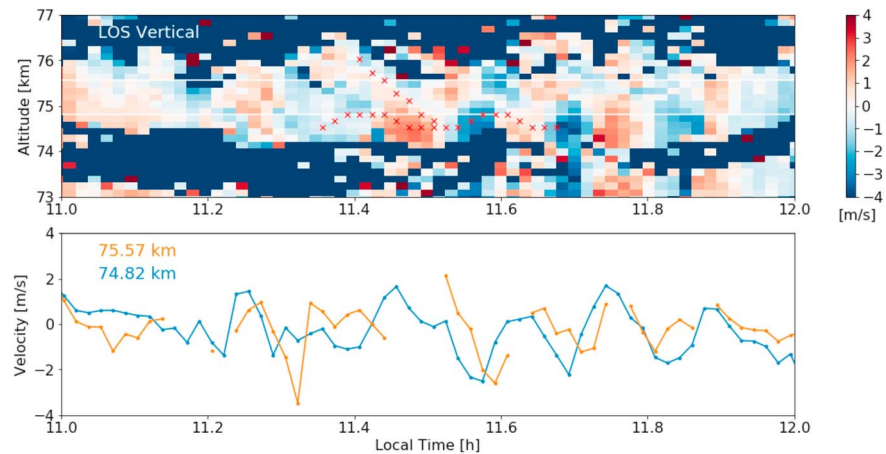


Figure 4. (top) Line-of-sight (LOS) velocities for vertical beam at 60-s resolution. (bottom) Velocities in vertical beam at two specific altitudes indicating phase shift. For more details see text.

the wave properties (see next section) we will concentrate on the interval between 11.4 and 11.6 LT where we have coherent oscillations for all four beams. This coherence suggests that the horizontal wavelength is larger than the beam separation but remains unspecified. In the next section we will estimate the horizontal wavelength based on the observed parameters and the GW dispersion relation.

Figure 4 shows again the LOS velocities for the vertical beam. The LOS velocities in the vertical beam are virtually identical to the vertical wind (see also Figure 5). The red crosses indicate the maximum reflectivity in part of the sinusoidal scattering layer and also in the downward sloping layer seen in Figures 1 and 2. At and below the narrow scattering layer, the vertical wind oscillates at a constant phase and with the same period of $T = 520$ s, but it leads the vertical displacement by 120 s or $\sim 90^\circ$ (Figures 1 and 2). This is expected if we assume a simple harmonic motion $w(t) = dz/dt \sim (d/dt) z_0 \sin \omega t = \omega z_0 \cos \omega t = \omega z_0 \sin(\omega t + \pi/2)$. The observed maximum vertical speed of 2–3 m/s is consistent with ωz_0 using the amplitude $z_0 = \frac{1}{2} \cdot 450$ m shown in Figure 1. The bottom panel of Figure 3 shows the wind at 74.82 km (blue line) and at 75.57 km (orange line). This is consistent with the assumption that just above the scattering layer the phase of the vertical wind descends in time consistent with an upward propagating wave (although data indicate possible evidence for standing wave features, as well, which are discussed in section 4.1). It is also interesting to note that the downward sloping line of maximum scattering (marked by the red crosses) coincides approximately with the phase for zero vertical wind.

Figure 5 shows the three components of the wind calculated from the linear combination of the four LOS components and rotation into geographic coordinates (K. Lee, personal communication, 2018). The time axis is the same as in the previous figures, but the vertical range extends from 66 to 77 km, well below the sinusoidal layer at 75 km. The zonal wind is mostly eastward during this hour. This is highlighted in the median values for the period from 11.4 to 11.6 LT, which vary between 20 and 40 m/s, and are shown on the right. The red lines are the standard deviation for each height with more than four data points during this 12-min interval. The meridional component is southward between 68 and 75 km with a relative maximum of ~ 50 m/s near 71 km. Above 75 and below 68 km, the meridional component is close to 0. At the top of this domain, the wind has a small northward component. Therefore, there exists a strong meridional wind shear of $\sim 40 \text{ m}\cdot\text{s}^{-1}\cdot\text{km}^{-1}$ (which with a typical $N^2 \sim 4 \times 10^{-4} \text{ s}^{-2}$ results in an unstable Richardson number $Ri = \frac{1}{4}$)

The vertical winds include the pattern that was already shown in Figure 4 and demonstrates that the standing oscillatory pattern extends from 75 km down to 68 km throughout the region of southward meridional winds. The average vertical wind is approximately 0, but individual profiles near 11.45 and 11.55 LT (marked by the red and blue dots in Figure 5, bottom) emphasize the periodic change in direction. Vertical speeds are small (below 1 m/s) at 69 km and grow to maximum values (2 to 3 m/s) at the interface layer at 75 km; these variations are consistent with growth due to decreasing ambient density.

The horizontal winds were derived under the assumption that the wind field is homogeneous across all four beams, that is, over a separation of up to 6 km. This is much smaller than in the experiment at Arecibo,

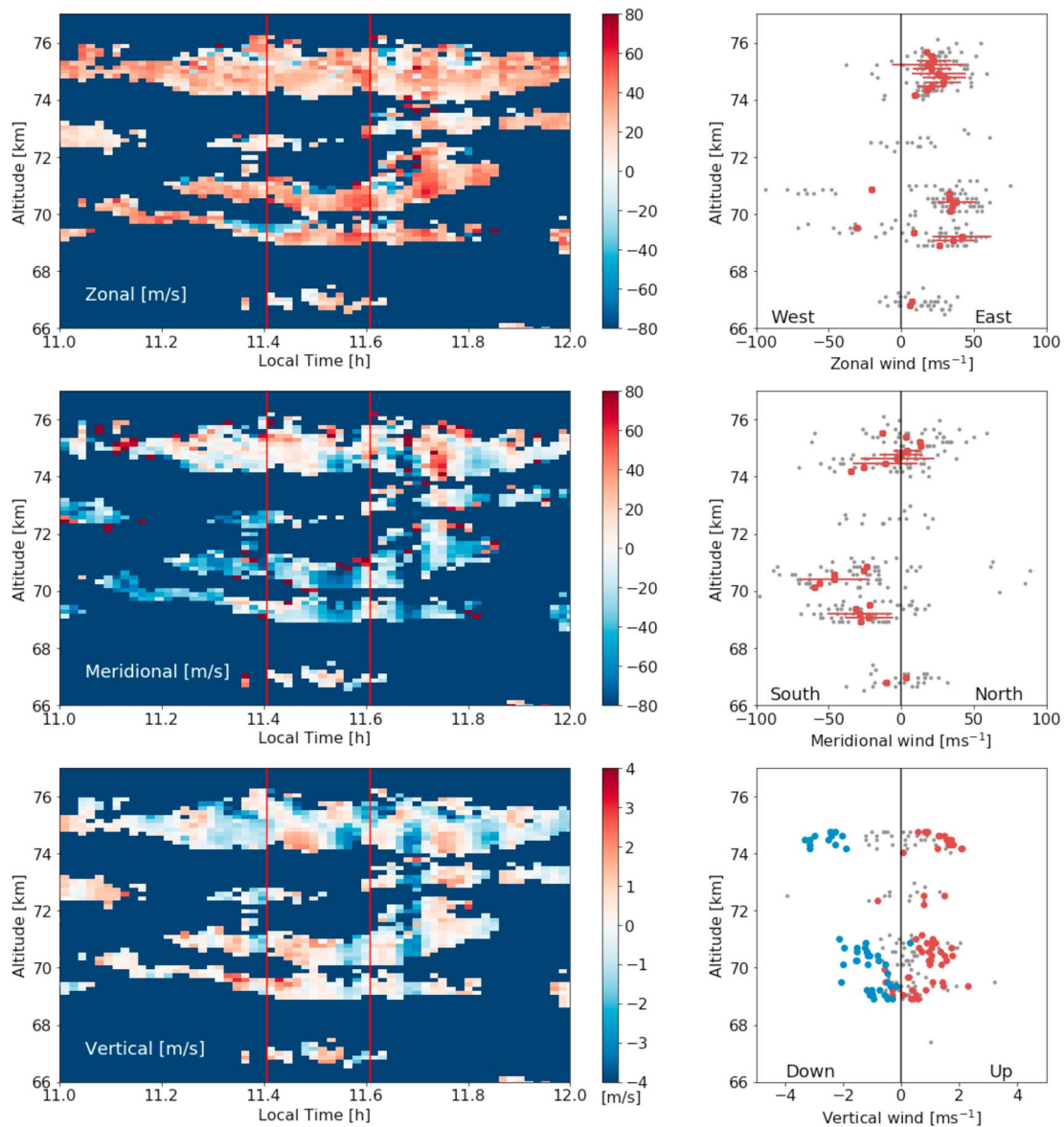


Figure 5. (left column) Zonal, meridional, and vertical wind components for same time interval, but for altitudes 66–77 km. (right column) Individual data points and median wind profiles for zonal, meridional, and vertical components. Details see text.

where the beam separation was 14 km. Fritts and Janches (2008) observed out-of-phase oscillations between the LOS velocities and explained that they were caused by out-of-phase horizontal wind fluctuations from a GW motion with short horizontal wavelength of at least 28 km and trapped in a Doppler duct. While our mean horizontal winds are largely consistent within the 1-hr period presented here, we must understand the large variance and oscillatory pattern, especially in the layers at 70 and 72 km after 11.6 LT. It has been known for many years that vertical wind fluctuations may introduce errors and biases to horizontal wind measurements (Kudeki et al., 1993). This is especially the case for Doppler beam wind measurements at Jicamarca due to the very small off-zenith angles (Fritts et al., 1992). For example, a 1-m/s LOS wind in a 2.5° off-zenith beam can be caused by a 1-m/s vertical wind or a 22-m/s horizontal wind. Such fluctuations in the horizontal wind components match also our observations. Therefore, we use the horizontal wind components only as estimate for the mean background wind profile, which is indicated by the red dots in Figure 5 (except for a few outliers).

4. Discussion and Modeling

4.1. Observed Wave Parameters

The observations suggest the presence of a quasi-monochromatic GW with apparent period $2\pi/\omega = 520$ s. Based on the vertical winds, below 75 km, the wave has a very long vertical wavelength (evanescent or near evanescent) or is likely ducted. Above 75 km, a wave emerges with the same period and a very short vertical wavelength of $\lambda_z = 2\pi/m = 2.2$ km, that again may also likely be subject to ducting due to reflections at higher altitudes—indeed, there is some evidence of standing wave structure in the vertical wind field in Figure 5, bottom panel, visible about ~ 75 km and 11.6 LT. We also know the horizontal background wind profile, and, in the following, we try to explain the observations based on the dispersion relation for linear GW. This is further demonstrated by a numerical simulation that tests the hypothesized interpretation, for comparison with data.

The local vertical wavenumber m of a GW with intrinsic frequency $\hat{\omega}$ (with $\hat{\omega}^2 > f^2$) can be calculated from the Taylor-Goldstein equation (Nappo, 2012):

$$m^2 = \frac{N^2 k^2}{\hat{\omega}^2} + \frac{k}{\hat{\omega}} \frac{d^2 u_0}{dz^2} - \frac{1}{H} \frac{k}{\hat{\omega}} \frac{du_0}{dz} - k^2 - \frac{1}{4H^2} \quad (1)$$

where $N^2 = (g/T)(dT/dz + \Gamma_{ad})$ is the buoyancy frequency and $H = RT/(Mg)$ is the pressure scale height. The wave is propagating horizontally with wave number k , and u_0 is horizontal wind component along the propagation direction. The intrinsic wave frequency is Doppler shifted as

$$\hat{\omega} = \omega - u_0 k \quad (2)$$

and the horizontal phase speed in propagation direction is $\hat{c} = c - u_0 = \omega/k - u_0$. N^2 and H can be estimated from the MSIS model for the particular time and location (Picone et al., 2002). At 74 km, we find $T_B = 2\pi/N = 316$ s and $H = 6.2$ km, and for the following estimation, we treat these parameters as constants.

The second and third terms in the dispersion relation include the wind curvature and wind gradient along the propagation direction. They are equal to zero for constant background wind; however, for small-scale GWs and strongly varying background winds, like in our case, they are important for determining vertical propagation. The last term is usually small compared to the other terms. To quantify our statements about the different terms, we use the observed $\omega = 2\pi/520$ s and horizontal wind profiles and, as reasoned below, northward wave propagation with $k = 2\pi/16$ km. For 75.5 km and meridional wind 15 m/s, the five terms in equation (1) are $1.7 \cdot 10^{-6}$, $-3.1 \cdot 10^{-7}$, $-5.6 \cdot 10^{-8}$, $-1.5 \cdot 10^{-7}$, and $6.5 \cdot 10^{-9} \text{ m}^{-2}$, respectively. For this set of parameters, the first term is dominant and $m^2 = 1.2 \cdot 10^{-6} \text{ m}^{-2}$, corresponding to a vertically propagating wave. Note that the vertical wavenumber and wavelength depend strongly on the choice of k and u_0 via the term $(\frac{\omega}{k} - u_0)^2$ in the denominator of the leading term. Here it is only important that $m^2 > 0$ in a narrow region above 75 km.

Next, we argue that the observed short wave period must be strongly Doppler shifted. To illustrate this, let us assume that there was no background wind. In this case, $m^2 = \frac{N^2 k^2}{\omega^2} - k^2 + \frac{1}{4H^2}$, and, with observed m and ω , the horizontal wavelength would be only 2.8 km, or $k = 2\pi/(2.8 \text{ km})$. Such a short wavelength contradicts the fact that the four horizontally spaced beams observed no significant phase shift in the wave pattern.

Now we assume that wave propagation is purely in zonal direction (which we will contradict). From Figure 4 we estimate a zonal background wind of about +25 m/s. The dispersion relation suggests that for a vertical wavelength of 2.2 km (derived from the phase line), the horizontal wavelength should be ~ 16 km. However, the zonal background wind is positive and relatively constant throughout the region from 66 to 76 km, while we clearly see the vertical wave propagation change at 75 km. Therefore, we conclude that the horizontal wave vector must have a meridional component and the wave propagation responds to the changing meridional background wind. A meridional propagation is also consistent with the observed differences in the echoes from the south beam compared to the other beams (Figure 2).

From Figure 5, we notice a small northward component of the horizontal wind above 75 km, where the wave exhibits vertical phase progression. The dispersion relation yields for pure meridional propagation and values $u_0 = +15$ m/s and $\lambda_h \sim 11$ km, the approximate measured value for the vertical wavelength, 2.2 km. However, the wave vector may also include a small zonal component. For example, with both background wind components, as estimated above, a wave with horizontal wavelength 14.9 km and

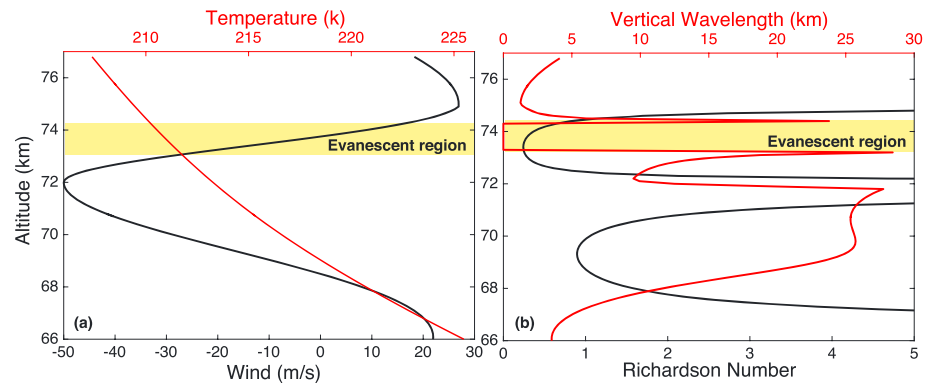


Figure 6. Profiles of (a) horizontal wind and temperature used for the model simulations, along with (b) estimated vertical wavelength and Richardson number, showing layer of evanescence and near instability.

propagating 17° clockwise from north would also match the observed vertical wavelength of 2.2 km. Unfortunately, we cannot fully specify both wavenumber components based on our limited radar observations. Depending on propagation azimuth, horizontal wavelengths between 14 and 20 km appear plausible. For simplification of the modeling study, we assume a northward propagating wave with $\lambda_h = 16$ km and $c = \lambda_h/T = \omega/k_h = +30.8$ m/s.

The observed meridional wind profile between 67 and 75 km contains a strong southward jet, leading to (when combined with typical temperature profiles) a region of evanescence (i.e., $m^2 < 0$) between 73 and 74 km that contributes to the reflection and ducting of the GWs (Nappo, 2012). Also note that the wave phase speed c is always larger than $u_0(z)$, so that critical levels are not encountered outside of the opposing wind jet. In order to evaluate the vertical propagation, the curvature term of the dispersion relation must be included. It provides positive values for m^2 near the maximum of the wind jet, so that upward and downward propagation of wave energy can occur, forming a standing wave pattern between 66 and 74 km with large vertical wavelength when subject to evanescence and reflection ~ 74 km.

4.2. Modeling Results

We further examine the wave propagation with help of a numerical model, using an idealized wind profile that is fit approximately to data. A nonlinear, two-dimensional numerical model was used to simulate the observed GW processes (Snively et al., 2013; Snively & Pasko, 2008, and references therein). The model has been used extensively to investigate the propagation, dissipation, and interaction of GWs in the mesosphere and lower thermosphere and for comparisons with observed data (Cao et al., 2016; Heale et al., 2014; Simkhada et al., 2009). The background meridional wind profile (Figure 5) was modeled with a Gaussian centered at 71 km, a maximum southward wind of 50 m/s, and turning northward below 69 and above 75 km. The temperature and buoyancy frequency profile were taken from the MSIS model (Picone et al., 2002). It is noteworthy that a directly measured temperature structure would enable a higher fidelity simulation, but for the particular case the winds are sufficiently strong to dominate the evolution of the observed waves. Figure 6 shows the resulting wind and temperature profiles.

Figure 6 also shows the resulting propagation characteristics for the hypothesized wave of interest, revealed via vertical wavelength and Richardson number. While intuition might suggest that the strong opposing wind would be the primary cause for evanescence, both the gradient and also the thermal structure contribute to the wave's refraction and subsequent partial reflection beginning near 73 km (again, see vertical wavelength plotted in Figure 6). The red lines in the graphs of Figure 6b show the background-dependent vertical wavelength based on the dispersion relation. Ducting conditions exist between ~ 67 and 73 km (the inflection points of the wind profile, for which $\partial^2 u_0 / \partial z^2 = 0$, are at 69.3 and 73.4 km), bordered by a narrow upper region of evanescence ($m^2 < 0$) between 73 and 74 km. Above 75 km, the wave propagates vertically again and the vertical wavelength becomes smaller due to the changing background wind. As the wind changes northward, $(c - u_0)$ becomes smaller, and the first term in the dispersion relation causes m to grow (and the vertical wavelength to shrink).

Using a simple quasi-monochromatic source that generates a wave with the observed characteristics, we investigate the resulting measurable signatures in this environment. The wave was launched at 50-km

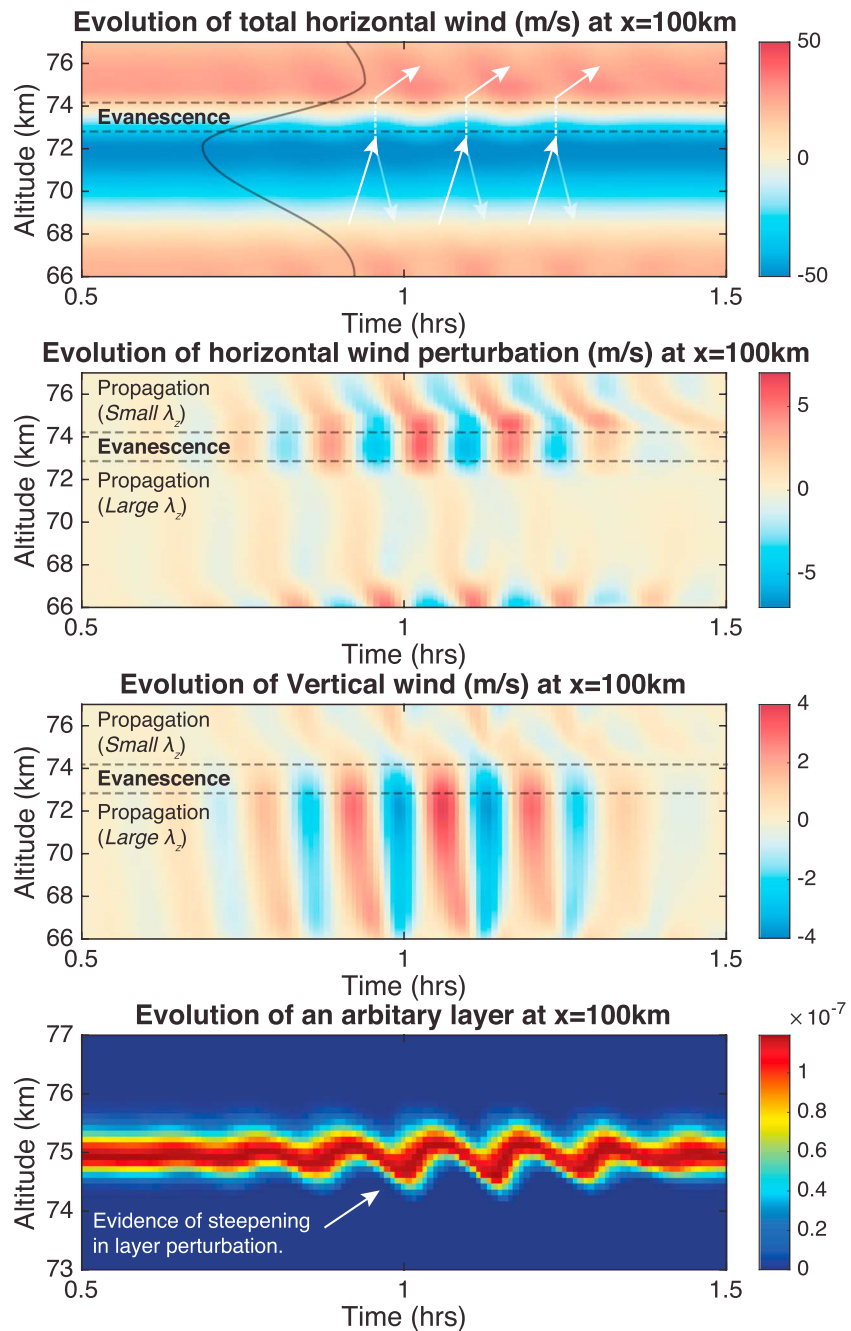


Figure 7. Modeling case with wave ducting, evanescence, and propagation into a region of stronger northward flow. Shown is the evolution of three wind parameters at a fixed location as they evolve over time: (a) total horizontal wind, (b) horizontal wind perturbation, and (c) vertical wind perturbation. Also shown are the perturbations to an idealized tracer layer (d) at ~75-km altitude.

altitude, with a 16-km horizontal wavelength, and a 520-s dominant period (locally, this leads to a ~15-km vertical wavelength); it propagates northward with $c = +31$ m/s opposite to the southward wind jet. Figure 7 shows simulated background wind (a), horizontal (b), and vertical (c) wind perturbations as sampled at a fixed horizontal location along the propagation path as they evolve over time. Also shown are the resulting density perturbations to a prescribed layer in panel (d), which exhibits evidence of slight nonlinearity; the displacement amplitudes are approximately consistent with those measured. Note that this layer is specified ideally to visualize the vertical perturbations imposed by the wave and is not consistent with a physical scattering layer. These features (in velocity and displacement) agree reasonably with the data and support the

interpretation that the waves observed are passing through a region of near evanescence, below which they are likely ducted. At higher altitudes, above the stable region $\sim 75\text{--}76$ km, the model again finds reduced stability, which may increase tendency toward partial reflection; while this cannot be confirmed due to unavailability of data, the measured vertical velocity in Figure 5 also shows some evidence for standing wave features at 75-km altitude. The differing amplitudes of horizontal wind perturbations in model versus data are consistent with the likely error associated with the measurement of the short-period wave dynamics, as discussed above.

It may be reasonable to speculate that the observed waves could have been generated in situ by larger-scale (wave) dynamics, for example, Heale et al. (2017), noting that the Richardson number is rather low in the shear layer ~ 74 km, as seen in Figure 6b above the layer through which the wave was evanescent. However, the data are insufficient to determine this, as they exhibit considerable variability due to the state of the scattering regions that precludes assessments of larger-scale dynamics. The particular event is quite coherent and has a horizontal scale large enough to be reasonably explained as an ambient ducted gravity wave propagating through the vertically structured atmosphere. Thus, both data and modeling support that the wave is tunneling through a region of evanescence and entering a second more stable region above ~ 74 km, where it may continue to propagate freely and/or become subject to partial reflection by mesopause region structure.

The simulations also demonstrate how vertical wind amplitudes are large in the less stable ducting region below the layer of evanescence and weaker (in accordance with the polarization relation) for more stable regions through which they propagate above. This agrees with our wind data (Figure 5); however, the transition is much sharper in our observations than in the model, which uses relatively smooth profiles. On the other hand, horizontal wind perturbations appear larger for the wave emerging from evanescence at higher altitudes than for the lower (ducted) wave in the model. Unfortunately, this cannot be compared definitively with our observations. While horizontal wind estimates are considered robust when averaged over half an hour, short-period horizontal wind fluctuations may be less accurate due to small off-zenith angles for all beams as explained above, especially in the presence of strong periodic vertical wind perturbations.

5. Summary and Conclusions

Short-period vertical wind oscillations in the mesosphere have been observed by VHF radar for a long time (Miller et al., 1978; Woodman & Guillen, 1974) and ducting of GWs at Jicamarca radar has been first suggested by Fritts et al. (1992). This is the first detailed study of a short-period GW at Jicamarca as it encounters varying background conditions causing a drastic change in vertical wavelength and propagation.

Our observed wave parameters match typical results derived from airglow imaging, lidar, and modeling studies. The observed period was 520 s (8.7 min), the vertical wavelength for the propagating wave was as small as 2.2 km, and the horizontal wavelength was between 14 and 20 km. (We used 16 km for the modeling case.) While we are less certain about the propagation direction and phase speed, Simkhada et al. (2009) reported many examples of wave ducting with similar periods (8–11 min), horizontal wavelengths (16–20 km), and phase speeds (25–50 m/s). Our observations are consistent with this, and the GW dispersion relation, and also supported by model simulations. Overall, results suggest that the wave exhibited a short horizontal wavelength and propagated northward in a ducting region associated with a sheared wind flow.

Our case confirms that ducted waves are readily able to tunnel through regions of evanescence, leading to wave energy and momentum leaking into the layers above (e.g., where they may become dissipated or ducted). Fritts and Janches (2008) also presented clear evidence for wave ducting in the mesosphere based on wind measurements with the Arecibo radar, while other recent observations of mesospheric wave ducting come from nighttime airglow and lidar techniques (Bossert et al., 2014; Cao et al., 2016). The discovery of this event was made possible by studying Jicamarca mesospheric echoes at 8.64-s resolution, which has not been done in the previous studies. The combination of backscatter signal and wind profiles was crucial in detecting the behavior of the wave at the ducting interface. The observation of a thin, modulated layer and vertical phase propagation is distinct from the other processes often observed in mesospheric echo layers, which have been attributed to Kelvin-Helmholtz instabilities (Lehmacher et al., 2007). On the other hand, the dynamics measured at the top of the layer, where the GW vertical scales are reduced by northward flow and varied stability, also revealed evidence for weakly nonlinear wave dynamics that may have contributed to turbulence and the 3-m-scale irregularities that contribute to radar scattering. While mesospheric layers

present a rich laboratory for small-scale wave and instability dynamics, these daytime interpretations could be much aided by high-resolution observations of other parameters, such as temperatures and electron densities.

Acknowledgments

G. Lehmacher was supported by NSF grant AGS-1143514. E. Kudeki, P. Reyes, and K. Lee were supported by NSF grant AGS-1143523. The authors have stated no conflicts of interest. The data are available at the http://remote2.ece.illinois.edu/MST_ISR_EEJ_V3 website. G. L. appreciates valuable discussions with J. Chau. C. J. Heale, and J. B. Snively were supported under NASA grant 80NSSC18K1037 to Embry-Riddle. We thank the staff of the Jicamarca Radio Observatory for their excellent work in operating the radar and collecting data. The Jicamarca Radio Observatory is a facility of the Instituto Geofísico del Perú operated with support from the NSF grant AGS-1433968 through Cornell University.

References

- Bossert, K., Fritts, D. C., Pautet, P. D., Taylor, M. J., Williams, B. P., & Pendleton, W. R. (2014). Investigation of a mesospheric gravity wave ducting event using coordinated sodium lidar and Mesospheric Temperature Mapper measurements at ALOMAR, Norway (69° N). *Journal of Geophysical Research: Atmospheres*, *119*, 9765–9778. <https://doi.org/10.1002/2014JD021460>
- Cao, B., Heale, C. J., Guo, Y., Liu, A. Z., & Snively, J. B. (2016). Observation and modeling of gravity wave propagation through reflection and critical layers above Andes Lidar Observatory at Cerro Pachón, Chile. *Journal of Geophysical Research: Atmospheres*, *121*, 12,737–12,750. <https://doi.org/10.1002/2016JD025173>
- Chandran, A., Rusch, D., Palo, S., Thomas, G., & Taylor, M. (2009). Gravity wave observations in the summertime polar mesosphere from the cloud imaging and particle size (CIPS) experiment on the aim spacecraft. *Journal of Atmospheric and Solar-Terrestrial Physics*, *71*(3), 392–400. <https://doi.org/10.1016/j.jastp.2008.09.041>
- Chimonas, G., & Hines, C. O. (1986). Doppler ducting of atmospheric gravity waves. *Journal of Geophysical Research*, *91*, 1219–1230.
- Eckart, C. (1961). Internal waves in the ocean. *Physics of Fluids*, *4*, 791–799. <https://doi.org/10.1063/1.1706408>
- Fritts, D. C., & Janches, D. (2008). Dual-beam measurements of gravity waves over Arecibo: Reevaluation of wave structure, dynamics, and momentum fluxes. *Journal of Geophysical Research*, *113*, D05112. <https://doi.org/10.1029/2007JD008896>
- Fritts, D. C., & Yuan, L. (1989). An analysis of gravity wave ducting in the atmosphere: Eckart's resonances in thermal and doppler ducts. *Journal of Geophysical Research*, *94*(D15), 18,455–18,466.
- Fritts, D. C., Yuan, L., Hitchman, M. H., Coy, L., Kudeki, E., & Woodman, R. F. (1992). Dynamics of the equatorial mesosphere observed using the Jicamarca MST radar during June and August 1987. *Journal of the Atmospheric Sciences*, *49*, 2353–2371.
- Guo, L., Lehmacher, G. A., Kudeki, E., Akgiray, A., Sheth, R., & Chau, J. (2007). Turbulent energy dissipation rates and eddy diffusivities in the tropical mesosphere obtained from Jicamarca radar data. *Advances in Space Research*, *40*, 744–750. <https://doi.org/10.1016/j.asr.2007.05.068>
- Heale, C. J., Bossert, K., Snively, J. B., Fritts, D. C., Pautet, P.-D., & Taylor, M. J. (2017). Numerical modeling of a multiscale gravity wave event and its airglow signatures over Mount Cook, New Zealand, during the DEEPWAVE campaign. *Journal of Geophysical Research: Atmospheres*, *122*, 846–860. <https://doi.org/10.1002/2016JD025700>
- Heale, C. J., Snively, J. B., & Hickey, M. P. (2014). Numerical simulation of the long-range propagation of gravity wave packets at high latitudes. *Journal of Geophysical Research: Atmospheres*, *119*, 11,116–11,134. <https://doi.org/10.1002/2014JD022099>
- Hickey, M. P. (2001). Airglow variations associated with nonideal ducting of gravity waves in the lower thermosphere region. *Journal of Geophysical Research*, *106*(D16), 17,907–17,917. <https://doi.org/10.1029/2001JD900182>
- Hoppe, U.-P., & Fritts, D. C. (1995). High-resolution measurements of vertical velocity with the European incoherent scatter VHF radar: 1. Motion field characteristics and measurement biases. *Journal of Geophysical Research*, *100*(D8), 16,813–16,825. <https://doi.org/10.1029/95JD01466>
- Isler, J. R., Taylor, M. J., & Fritts, D. C. (1997). Observational evidence of wave ducting and evanescence in the mesosphere. *Journal of Geophysical Research*, *102*, 26,301–26,313.
- Kudeki, E., Rastogi, P. K., & Sürücü, F. (1993). Systematic errors in radar wind estimation: Implications for comparative measurements. *Radio Science*, *28*(2), 169–179. <https://doi.org/10.1029/92RS01931>
- Lehmacher, G. A., Guo, L., Kudeki, E., & Chau, J. (2007). High-resolution observations of mesospheric layers with the Jicamarca VHF radar. *Advances in Space Research*, *40*, 734–743.
- Lehmacher, G. A., Kudeki, E., Akgiray, A., Guo, L., Reyes, P., & Chau, J. (2009). Radar cross sections for mesospheric echoes at Jicamarca. *Annales Geophysicae*, *27*, 2675–2684.
- Miller, K. L., Bowhill, S. A., Gibbs, K. P., & Countryman, I. D. (1978). First measurements of mesospheric vertical velocities by VHF radar at temperate latitudes. *Geophysical Research Letters*, *5*, 939–942. <https://doi.org/10.1029/GL005i011p00939>
- Nappo, C. (2012). *An introduction to atmospheric gravity waves*. Amsterdam: Academic Press.
- Nielsen, K., Taylor, M. J., Hibbins, R. E., Jarvis, M. J., & Russell III, J. M. (2012). On the nature of short-period mesospheric gravity wave propagation over Halley, Antarctica. *Journal of Geophysical Research*, *117*, D05124. <https://doi.org/10.1029/2011JD016261>
- Pautet, P., Taylor, M., Liu, A., & Swenson, G. (2005). Climatology of short-period gravity waves observed over northern Australia during the Darwin Area Wave Experiment (DAWEX) and their dominant source regions. *Journal of Geophysical Research*, *110*, D03S90. <https://doi.org/10.1029/2004JD004954>
- Pautet, P.-D., Taylor, M. J., Snively, J. B., & Solorio, C. (2018). Unexpected occurrence of mesospheric frontal gravity wave events over south pole (90°S). *Journal of Geophysical Research: Atmospheres*, *123*, 160–173. <https://doi.org/10.1002/2017JD027046>
- Picone, J. M., Hedin, A. E., & Drob, D. (2002). NRLMSISE-00 empirical model of the atmosphere: Statistical comparisons and scientific issues. *Journal of Geophysical Research*, *107*(A12), 1468. <https://doi.org/10.1029/2002JA009430>
- Sheth, R., Kudeki, E., Lehmacher, G., Sarango, M., Woodman, R., Guo, L., & Reyes, P. (2006). A high-resolution study of mesospheric fine structure with the Jicamarca MST radar. *Annales Geophysicae*, *24*, 1281–1293.
- Simkhada, D. B., Snively, J. B., Taylor, M. J., & Franke, S. J. (2009). Analysis and modeling of ducted and evanescent gravity waves observed in the Hawaiian airglow. *Annales Geophysicae*, *27*, 3213–3224. <https://doi.org/10.5194/angeo-27-3213-2009>
- Snively, J. B., Nielsen, K., Hickey, M. P., Heale, C. J., & Moffat-Griffin, T. (2013). Numerical and statistical evidence for long-range ducted gravity wave propagation over Halley, Antarctica. *Geophysical Research Letters*, *40*, 4813–4817. <https://doi.org/10.1002/grl.50926>
- Snively, J. B., Nielsen, K., Hickey, M. P., Heale, C. J., Taylor, M. J., & Moffat-Griffin, T. (2013). Numerical and statistical evidence for long-range ducted gravity wave propagation over Halley, Antarctica. *Geophysical Research Letters*, *40*, 4813–4817. <https://doi.org/10.1002/grl50926>
- Snively, J. B., & Pasko, V. P. (2003). Breaking of thunderstorm-generated gravity waves as a source of short-period ducted waves at mesopause altitudes. *Geophysical Research Letters*, *30*(24), 2254. <https://doi.org/10.1029/2003GL018436>
- Snively, J. B., & Pasko, V. P. (2008). Excitation of ducted gravity waves in the lower thermosphere by tropospheric sources. *Journal of Geophysical Research*, *113*, A06303. <https://doi.org/10.1029/2007JA012693>
- Sutherland, B. R., & Yewchuk, K. (2004). Internal wave tunneling. *Journal of Fluid Mechanics*, *511*, 125–134.

- Taylor, M. J., Pendleton, W. R. Jr., Clark, S., Takahashi, H, Gobbi, D., & Goldberg, R. A. (1997). Image measurements of short-period gravity waves at equatorial latitudes. *Journal of Geophysical Research*, *102*(D22), 26,283–26,299.
- Walterscheid, R. L., Hecht, J. H., Vincent, R. A., Reid, I. M., Woithe, J., & Hickey, M. P. (1999). Analysis and interpretation of airglow and radar observations of quasi-monochromatic gravity waves in the upper mesosphere and lower thermosphere over Adelaide, Australia. *Journal of Atmospheric and Solar-Terrestrial Physics*, *61*, 461–478.
- Woodman, R. F., & Guillen, A. (1974). Radar observations of winds and turbulence in the stratosphere and mesosphere. *Journal of the Atmospheric Sciences*, *31*, 493–503.